On aggregation errors in atmospheric transport inversions

Thomas Kaminski,[1,2] Peter J. Rayner,[3] Martin Heimann,[4] and Ian G. Enting[3]

Abstract. This paper explores the consequences of resolution of surface fluxes on synthesis inversions of carbon dioxide. Synthesis inversion divides the Earth's surface into a set of regions and solves for the magnitudes of fluxes from these regions. The regions are generally quite large. By considering an inversion performed at the resolution of the underlying transport model we show that the aggregation to large regions can cause significant differences in the final results, with errors of the same order of magnitude as the fluxes themselves. Using a simple model, we derive an algorithm to reduce this error. This algorithm accounts for the extra data uncertainty that is caused by uncertainty in the small-scale flux components. In the spatial synthesis inversion this extra data uncertainty reaches a maximum value of 3.5 ppmv. Accounting for it can halve the aggregation error. We provide suggestions for dealing with this problem when high-resolution inversions are not feasible.

1. Introduction

One of the critical uncertainties in predicting the trajectory of the climate system is the prediction of radiative forcing. Since a major cause of variations in this forcing is changes in greenhouse gas concentration, it is important to predict the budgets of the major greenhouse gases. As demonstrated by *Enting et al.* [1994], a major uncertainty in such a prediction is the uncertainty in the current budget. Also, any attempt to manage, for example, the global carbon cycle will require detailed quantitative understanding of the regional fluxes of carbon to the atmosphere. For both these reasons, it is important to refine techniques to infer these fluxes.

One important technique for such inferences is the inverse determination of sources using atmospheric concentration measurements. In the last decade or so, there have been several such studies. Examples include *Keeling et al.* [1989], *Tans et al.* [1990], *Enting et al.* [1995], *Fan et al.* [1998], *Rayner et al.* [1999], and *Bousquet et al.* [1999] for CO_2 and *Fung et al.* [1991], *Brown* [1993], and *Hein et al.* [1997] for CH_4.

Although there have been other approaches, the most common (used by all the studies cited above) is usually termed synthesis inversion [*Enting et al.*, 1995]. In synthesis inversion the flux field is constructed as a linear combination of a set of patterns. The solution of the inverse problem then involves finding the coefficients multiplying each of the patterns. The patterns may be contiguous regions as in the work

---

[1] Max-Planck-Institut für Meteorologie, Hamburg, Germany.

[2] Now at FastOpt, Hamburg, Germany.

[3] Cooperative Research Centre for Southern Hemisphere Meteorology, CSIRO Atmospheric Research, Aspendale, Victoria, Australia.

[4] Max-Planck-Institut für Biogeochemie, Jena, Germany.

by *Rayner et al.* [1999] or regions reflecting some underlying similarity such as the biome classifications used by *Enting et al.* [1995]. The patterns also may have some prescribed internal structure, reflecting external knowledge of fluxes, e.g., *Fan et al.* [1998], who used net primary productivity to shape their terrestrial flux patterns. Finally, the patterns also contain temporal structure such as a prescribed seasonal cycle or monthly pulses. We shall refer to each of these space-time flux patterns as basis functions. To carry out any sort of inversion, we need to know the concentration arising from a given basis function when subject to atmospheric transport. We refer to this as the corresponding response function.

Response functions are normally calculated by using a basis function as an input to an atmospheric transport model. The response function is generated by sampling the output of the transport model at chosen observation locations. The matrix of response functions for the full set of basis functions is the Jacobian matrix for the problem and contains all the information about atmospheric transport relevant to a particular setup.

There are two problems caused by the a priori choice of basis functions. The first is an arbitrary limit on the information that can be returned by an inversion. Ideally, this limit would be set by the inversion procedure itself, a situation that will arise with a large enough number of basis functions. The second problem is that the structure chosen for the basis functions will determine the magnitudes returned by the inversion procedure. The problem is illustrated in Figure 1. Figure 1b depicts a schematic diagram of a Jacobian for the idealized configuration of two source regions and one observational site shown in Figure 1a. Since region 1 is more upwind of the site than region 2, the response to an emission S_1 at region 1 is smaller than to an equal emission S_2 at region 2. The Jacobian depicted in Figure 1b is based on separate response functions for both regions. As mentioned above, in many inversion studies, largescale flux patterns are prescribed. Figure 1c shows two examples of these flux patterns, i.e., combinations of fluxes in both regions. The interesting point is that both patterns yield the same response at the observational site, although the first pattern quantifies a net source and the other one a net sink. If we imagine two inversions based on either response function, they would derive net fluxes of opposite sign from a measured concentration at the site. Hence an error in the internal structure of the basis function can spoil our inversion result.

Figure 1.

Solving for the fluxes in both regions separately constitutes a way to avoid prescribing a fixed, potentially wrong pattern. Since the inverse problem of inferring two fluxes from one observation is underdetermined, a Bayesian approach (as sketched in section 2) can be used to stabilize such type of inversion. Again, a flux pattern, which is made up of prior estimates for the fluxes from both regions, is assumed, and the fluxes from both regions will be adjusted separately. In the case of a wrongly shaped pattern, which yields a mismatch to the observations, the necessary adjustment, in general, will primarily concern the flux region with the strong response, i.e., region 2, and, in contrast to a fixed pattern approach, only slightly change the flux from the badly observed region 1. In this sense, the Bayesian approach prevents us from an over-interpretation of the concentrations collected at sparse networks and thus is preferable in this situation.

Avoiding the aggregation according to fixed patterns, however, increases the number of basis functions, which is computationally inconvenient, if not impossible, for two main reasons: First, as traditionally computed, each response function requires a separate tracer calculation in an atmospheric transport model. For 25 spatial basis functions and 12 monthly pulses we need 300 runs of an atmospheric transport model for perhaps 3 years each. Even with relatively low model resolution this is computationally demanding. Second, the size of the inversion calculation itself is a problem. More basis functions mean more unknowns and larger matrices in the inversion calculation. Given these constraints, inversions with relatively large predefined regions will remain a common tool. We need techniques to account for and reduce the errors displayed in Figure 1. Such a method is the purpose of this paper.

Recently, using an adjoint method, *Kaminski et al.* [1999a] have demonstrated the efficient calculation of a set of basis functions at the resolution of their transport model, thus eliminating the first problem. Provided the observing network is decided in advance, they can compute 10,000 response functions for their transport model (TM2 [*Heimann*, 1995]) at the cost of < 100 response functions if computed by the conventional method. Of course, the cost of the actual inversion at this resolution remains. In two inversion studies based on these response functions *Kaminski et al.* [1999b] and *Houweling et al.* [1999] used only 1 year of data, representing an average. Inversions of many years of data at this spatial resolution require inversion techniques more sophisticated than the straightforward matrix inversions performed in the above mentioned studies. More generally, the methods used by *Kaminski et al.* [1999a] will allow us to generate higher-resolution Jacobian matrices than we can invert.

The high-resolution Jacobian gives us a tool for investigating the size of the aggregation error. We can do this by deriving a low-resolution Jacobian, quantifying the response to a number of basis functions that is typical for inversion studies. Then the difference between an inversion with the full Jacobian and one with the low-resolution Jacobian quantifies the aggregation error. Such an approach was used by

Peylin et al. [2000], who compared low- versus very low-resolution inversions. They generated significant errors due to this aggregation, a problem we can expect to be worse with our higher-resolution inversions.

Obviously, we would like to reduce such aggregation errors rather than merely characterizing them. An approach to this problem was described by *Trampert and Snieder* [1996], who proposed an algorithm for dealing with this that requires a high-resolution model. The algorithm is to compute an extra contribution to data error resulting from the uncertainty in the inhomogeneity of fluxes within resolved regions. We will discuss the extra data error and then apply this algorithm to the case of atmospheric CO_2 inversions.

The outline for the remainder of the paper is as follows: in section 2 we recall the Bayesian inversion technique and describe the aggregation to regions. In section 3 we quantify the aggregation error by comparing a high-resolution inversion to a number of low-resolution ones, with different forms of aggregation. In section 4 we introduce a simple box model and use the model to quantify the aggregation error and to demonstrate the algorithm to reduce it. In section 5 we return to the three-dimensional model. Section 5 quantifies the extra error on the data side that accounts for the uncertainty in the unresolved small-scale fluxes and then applies the algorithm to the aggregation error. Finally, we make some recommendations about performing low-resolution inversions based on our experience. The appendix gives a step-by-step recipe for applying the algorithm. It should be possible to apply the algorithm even if all the detail of the two-box calculations proves difficult.

2. Bayesian Synthesis Inversion and Aggregation

In a Bayesian synthesis inversion for a flux field of a passive tracer we start with a prior estimate of fluxes $\mathbf{s_0}$, data $\mathbf{d_0}$, uncertainties for both quantified by the respective covariance matrices, $\mathbf{C}(s_0)$ and $\mathbf{C}(d_0)$, and finally a linear operator, the Jacobian of the problem, $\mathbf{J}$, that maps fluxes to data. We wish to estimate $\mathbf{s}$ such that the function

$$\begin{aligned} J = \quad {}^1\!/_2 \quad & [(\mathbf{Js} - \mathbf{d})^T \mathbf{C}(d_0)^{-1} (\mathbf{Js} - \mathbf{d}) \\ & + (\mathbf{s} - \mathbf{s_0})^T \mathbf{C}(s_0)^{-1} (\mathbf{s} - \mathbf{s_0})] \end{aligned} \tag{1}$$

is minimized, i.e., to match fluxes and data as closely as possible but taking account of the quality of our prior estimates and data. It can be simply shown [*Tarantola*, 1987] that (1) is minimized by

$$\hat{\mathbf{s}} = \mathbf{s_0} + \mathbf{J}^{-1}(\mathbf{d_0} - \mathbf{J s_0}) \quad , \tag{2}$$

where $\mathbf{J}^{-1}$, the generalized inverse of $\mathbf{J}$, is given by

$$\mathbf{J}^{-1} = [\mathbf{J}^T \mathbf{C}(d_0)^{-1} \mathbf{J} + \mathbf{C}(s_0)^{-1}]^{-1} \mathbf{J}^T \mathbf{C}(d_0)^{-1} . \tag{3}$$

For our demonstration of the aggregation error in section 4.3.1 to be as simple as possible, we will apply a non-Bayesian inversion. That is, we do not assume any prior knowledge about the fluxes. This can be considered a special case of (2), with $\mathbf{C}(s_0)$ tending to infinity; the respective expressions are

$$\hat{\mathbf{s}} = \mathbf{J}^{-1}\mathbf{d_0} \tag{4}$$

$$\mathbf{J}^{-1} = [\mathbf{J}^T\mathbf{C}(d_0)^{-1}\mathbf{J}]^{-1}\mathbf{J}^T\mathbf{C}(d_0)^{-1}. \tag{5}$$

In (3) and (5) the uncertainty on the data side $\mathbf{C}(d_0)$, whose inverse weights the data, is the sum of the uncertainties of both observations and model [*Tarantola*, 1987]:

$$\mathbf{C}(d_0) = \mathbf{C}(d_{0,\text{obs}}) + \mathbf{C}(d_{0,\text{mod}}) \quad . \tag{6}$$

Throughout this paper we wish to consider what happens when we move from a relatively high-resolution version of the problem to a reduced one, presumably for computational reasons. In the real cases later, $\mathbf{s}$ will initially have 864 spatial components corresponding to the number of surface grid points in the transport model TM2 [*Heimann*, 1995]. We will aggregate these to produce cases of 18 components (a 9×6 grid cell aggregation) or 54 components (a 4×4 grid cell aggregation). These aggregations are determined by the chosen sets of 18 (or 54) basis functions. To perform an inversion that (based on (2)) infers the multipliers α of these basis functions, we need a prior estimate for these multipliers and a covariance matrix of their uncertainties. These quantities are determined by their counterparts on the TM2 grid. The respective formulas become simple, if we normalize the 18 (or 54) basis functions such that $\mathbf{B}^T\mathbf{C}(s_0)^{-1}\mathbf{B} = 1$, where the columns of $\mathbf{B}$ are composed of the basis functions. In our case (though not necessarily), basis functions occupy disjoint regions. Thus any grid point belongs to only one basis function. Hence this normalization is readily achieved by multiplying every basis function with the appropriate scaling factor.

To find the priors for the multipliers we carry out an optimal fit for the low-resolution basis functions to the prior estimate for sources. We can use (4), with $\mathbf{B}$ taking the role of $\mathbf{J}$ and $\mathbf{C}(s_0)$ that of $\mathbf{C}(d_0)$, to yield

$$\alpha_\mathbf{0} = [\mathbf{B}^T\mathbf{C}(s_0)^{-1}\mathbf{B}]^{-1}\mathbf{B}^T\mathbf{C}(s_0)^{-1}\mathbf{s_0} = \mathbf{B}^T\mathbf{C}(s_0)^{-1}\mathbf{s_0} \tag{7}$$

and the covariance of their uncertainties

$$\mathbf{C}(\alpha_\mathbf{0})^{-1} = \mathbf{B}^T\mathbf{C}(s_0)^{-1}\mathbf{B} = 1 \quad , \tag{8}$$

in which we have exploited the normalization of the basis functions. (The non-Bayesian form is appropriate to infer the prior $\alpha_\mathbf{0}$ and its uncertainty, since a priori we do not have any knowledge about the multipliers.)

Inserting these quantities and the low-resolution Jacobian $\mathbf{J_B} = \mathbf{JB}$ in (2) and (3) finally solves for the multipliers, while the data side remains unchanged.

Some of the most important quantities inferred by inversion studies are the regionally averaged fluxes. In sections 3 and 5 we will compare the regionally averaged fluxes inferred by low-resolution inversions to those inferred by an inversion on the TM2 grid. In one case we first aggregate and then invert, while in the other we reverse the order of these operations. Denoting the averaging operator for region i by $\mathbf{A}_i$, the difference in the average flux for region i is

$$\begin{aligned} \Delta\hat{\mathbf{s}} &= \mathbf{A}_i\mathbf{B}[\alpha_\mathbf{0} + \mathbf{J_B}^{-1}(\mathbf{d_0} - \mathbf{J_B}\alpha_\mathbf{0})] \\ &\quad -\mathbf{A}_i[\mathbf{s_0} + \mathbf{J}^{-1}(\mathbf{d_0} - \mathbf{J}\mathbf{s_0})]. \end{aligned} \tag{9}$$

3. Demonstration of the Effect

The goals of this section are to demonstrate and better understand the effect of aggregation in the flux space on the result of inversions. We investigate the impact both of the degree of aggregation and of the various details that influence the aggregation. The essential tool for these inversions is the Jacobian matrix of TM2. TM2 [*Heimann*, 1995] is one of the three-dimensional atmospheric transport models typically used for biogeochemical studies [*Law et al.*, 1996; *Denning et al.*, 1999] including inversion of the atmospheric transport [*Hein et al.*, 1997; *Bousquet et al.*, 1999]. For a typical observational network the full Jacobian matrix, i.e., the one quantifying the response of the fluxes resolved on the full model grid, can be efficiently computed by means of the model's adjoint [*Kaminski et al.*, 1999a], which has been generated by the Tangent linear and Adjoint Model Compiler (TAMC (R. Giering, 1997, available at http://puddle.mit.edu/~ralf/tamc)).

First, to better understand the mechanism causing aggregation error, we resume the discussion of Figure 1. For aggregation error to appear, two criteria must be fulfilled. First, the response functions for both regions must differ. Recall that the errors we are concerned with are in small-scale structure. In the case of Figure 1 these are errors in the difference of fluxes between the two regions. If the responses were the same from both regions then such errors would not be observable and would not damage our inversion. Second, sampling must be inhomogeneous. We can already see this in the case shown in Figure 1 where the inversion for the large region is biased toward the more strongly observed sub-region. We will show this more clearly in section 4.

Figure 2.

That the first criterion applies to our type of inversion study is suggested by Figure 2. Figure 2 quantifies the sensitivity of the January concentration at station Point Barrow in Alaska (see location of the cross) to surface fluxes in the same month at all grid points. Figure 2 clearly shows that, e.g., the sensitivity to fluxes over North America is far from uniform. Second, inhomogeneous sampling is inevitable since typical networks comprise less than 100 sites, while even a coarse resolution model like TM2 has $\sim$800 spatial flux components.

As described in section 2, all inversions presented here are set up as Bayesian synthesis inversions. Except for details of aggregation, their setups are almost identical to the standard setup of *Kaminski et al.* [1999b]; they infer a cyclostationary CO_2 surface flux field (12 monthly means at each TM2 surface grid cell) from a quasi-stationary seasonal cycle, which they have fitted to observations at 25 observational sites (12 monthly means at each site). The observations span the period 1981–1986 and were provided by the National Oceanic and Atmospheric Administration Climate Monitoring and Diagnostics Laboratory (NOAA-CMDL) [Globalview–CO2, 1996]. They use prior flux estimates and uncertainties based on process models of the ocean and the terrestrial biosphere as well as on statistics of fossil fuel burning and land use change. The data uncertainties are the residuals to the fit of the quasi-stationary seasonal cycle and are meant to account for all variability in the data that the cyclostationary model setup cannot mimic. We assume zero correlation among these uncertainties.

The only detail in which our reference inversion R differs from their inversion is that we set a uniform (and uncorrelated) data uncertainty of 0.5 ppmv. A uniform uncertainty has been used by *Rayner et al.* [1999] as well, but they take the higher value of 0.7 ppmv in order to account for the additional uncertainty arising from uncertainty in fluxes they do not resolve. We will come back to this point in section 5.

Our reference inversion has the spatial resolution of the TM2 grid, i.e., 36 flux components in the zonal direction times 24 components in the meridional direction. For our standard experiments we aggregate every six components in the zonal direction and every eight components in the meridional direction (see Figure 3 for the blocks of aggregation). The components' prior estimates and their uncertainties are computed from the full-resolution values as described in section 2. To investigate the role of the flux pattern upon which the aggregation is based, we use either a pattern that is uniform over each region (case U18) as in the study of *Rayner et al.* [1999] or a pattern that is shaped like the prior estimate (case P18) as in the study of *Bousquet et al.* [1999].

Figure 3.

We will see later (section 5) that the aggregation error is closely related to weighting of the observations. To obtain a feeling for this interaction, we also modify both standard cases to have the nonuniform data uncertainties of *Kaminski et al.* [1999b]. These uncertainties range from 0.06 to 3.1 ppmv compared to the uniform 0.5 ppmv in our standard cases. The respective cases are denoted by U18W and

P18W. Finally, we want to explore the effect of the degree of aggregation on the error. In cases U54 and P54 we aggregate every four components in the zonal direction and every four components in the meridional direction, which yields 54 spatial components.

For the case U18, Figure 3 shows the aggregation errors in the annual means, which have been computed according to (9). Figure 3 (top) shows the fluxes for the 18 regions, inferred by the low-resolution inversion. The annual mean fluxes in Figure 3 (middle) are derived by aggregating the fluxes inferred by the full-resolution inversion R, i.e., the fluxes free from aggregation error. For convenience, Figure 3 (bottom) shows the amount by which the low-resolution inversion deviates from the high-resolution one. By and large, even in this annual mean representation the aggregation error dominates the fluxes derived by the full-resolution inversion. While the aggregated fluxes are in the range from –20 to 20 g C $m^{-2}yr^{-1}$, the aggregation error reaches values between –60 and 60 g C $m^{-2}yr^{-1}$.

Table 1.

Table 1 gives a few diagnostics of the aggregation error in the monthly mean fluxes. For all six cases introduced above, Table 1 shows the minimum and maximum error, the absolute maximum, as well as the root-mean-square (rms) error, both unweighted and area weighted. The most important diagnostics are probably the absolute maximum and the area-weighted rms, the first quantifying the maximum error caused by aggregation and the latter quantifying the over all error. The full-resolution inversion R infers fluxes from –463 g C $m^{-2}yr^{-1}$ to +190 g C $m^{-2}yr^{-1}$, which provides a scale to assess the magnitude of errors. In the U18 case the largest aggregation error in 1 month and region is approximately –900 g C $m^{-2}yr^{-1}$. The area-weighted rms error is $\sim$90 g C $m^{-2}yr^{-1}$. Depending on the size of the region, this corresponds to an average error of $\sim$ 2 Gt C yr^{-1} for each region. For all 18 region aggregations, using shaped patterns about halves the aggregation error, while in the 54 region case, using shaped patterns increases the error by $\sim$50%. This result is at first surprising since a more accurate match to the internal shape of the patterns should, generally, help the inversion, as is demonstrated by the two-box example in section 4. The critical point, however, is that lacking information about the true source shape, we had to use the shape of the a priori source to construct the patterns. While in the 18 region case this yields an improvement over the uniform pattern case, the uniform patterns are a more accurate match to the proper internal structure in the 54 region case than our a priori choice. It is only by considering the aggregation error that we can tell whether we succeeded in capturing the aspects of the small-scale structure that is relevant to the inversion.

Another related problem concerns inversions with non-uniform patterns, in general. For uniform patterns any unresolved small-scale structure has zero sum and so, given the diffusive nature of atmospheric transport, is unlikely to be observed far from its region. For non-uniform patterns this does not hold. The impact of this effect on an inversion will depend on the magnitudes of the unresolved sources and their concentration signatures in the observing network. The converse of this argument is that the resolved non-uniform patterns do not estimate average fluxes from regions. This negative consequence offsets some of the advantages of using non-uniform (but hopefully more correct) patterns.

Moving from 18 to 54 regions clearly reduces the aggregation error as one would hope. Finally, using the data uncertainty, which is derived from interannual variability (cases U18W and P18W), reduces the error considerably as compared to uniform data uncertainty. We will further discuss this point in section 5.

4. Simple Example for the Effect

In this section we use a simple example to improve our understanding of aggregation error. This error can be seen in a simple two-box model of the atmospheric transport when aggregating two hemispheric flux components. First, we describe the simple model and then perform a series of inversion experiments with varying setups, all of which are non-Bayesian to keep the example as simple as possible. Second, we will derive a recipe to reduce the aggregation error, which in section 5 will be applied to the three-dimensional model that we presented in section 3.

4.1. Two-Box Model

The two-box model that we employ is a familiar tool to transport modelers. For example, it has been employed by *Tans* [1997] and described in more detail by *Rayner et al.* [2000]. In the model, the concentration of an arbitrary tracer in each hemisphere (index 1 for the north and 2 for the south) evolves in time according to

$$\begin{aligned} \frac{M}{2}\frac{dc_1}{dt} &= s_1 - \frac{M}{2}\kappa(c_1 - c_2) \\ \frac{M}{2}\frac{dc_2}{dt} &= s_2 - \frac{M}{2}\kappa(c_2 - c_1) \ , \end{aligned} \tag{10}$$

where s_i denotes the sources (as emission rates) and κ is the exchange rate of air parcels between hemispheres as a fraction of the hemispheric air per time. M is the mass of the atmosphere and, for convenience, also absorbs the conversion factor from a mass mixing ratio (mass of tracer divided by mass of air) to a concentration. We reformulate (10) in terms of the average concentration, $c_+ = (c_1 + c_2)/2$, and the difference or gradient between the hemispheres, $c_- = c_2 - c_1$

as well as $s_+ = s_1 + s_2$ for the sum of the sources and $s_- = s_2 - s_1$ for their difference. This reformulation is most convenient because after this transformation of bases, the differential equations in (10) decouple and thus can be integrated separately. Assuming constant sources over a time interval Δt and, for convenience, no initial concentration difference, the changes in the average concentration and the difference are linearly related to the source difference and sum by

$$\begin{aligned} \Delta\vec{c} &= \begin{pmatrix} \Delta c_+ \\ \Delta c_- \end{pmatrix} \\ &= \begin{pmatrix} \frac{\Delta t}{M} & 0 \\ 0 & \frac{1}{M\kappa}(1 - e^{-2\kappa\Delta t}) \end{pmatrix} \begin{pmatrix} s_+ \\ s_- \end{pmatrix} \\ &= \mathbf{T}\vec{s} \ . \end{aligned} \tag{11}$$

We will see below that the size of the aggregation error depends on the magnitude of s_-. A large s_- component occurs for instance during the Northern Hemisphere summer. The prior CO$_2$ flux field for the inversions presented in section 3 yields a Northern Hemisphere sink of 5.5 Gt C for the period from June to August, and a Southern Hemisphere source of 0.5 Gt C. Using these numbers, a value of $M = 2.1$ Gt C ppmv^{-1}, and an exchange rate of $\kappa = 1$ yr^{-1}, (12) yields concentration changes of $\Delta c_+ = -2.4$ ppmv for the average and $\Delta c_- = -4.5$ ppmv for the difference. Whenever in the remainder of this section we give explicit numbers as examples, these are derived from the above values.

4.2. Sampling and Jacobian

Since the effect we intend to describe is caused by inhomogeneity of sampling, we assume an uneven distribution of sampling sites between the hemispheres: two stations in the north, Point Barrow (index B) and Mauna Loa (index M), and only one station in the south, South Pole (index S). This distribution among the hemispheres is close to that used in section 3, where we have 17 stations in the north and 8 in the south. The concentration changes at these stations are denoted by $\Delta c_B, \Delta c_M, \Delta c_S$. They can be computed from $\Delta\vec{c}$ by

$$\begin{aligned} \Delta\vec{c}_{\text{mod}} &= \begin{pmatrix} \Delta c_B \\ \Delta c_M \\ \Delta c_S \end{pmatrix} = \begin{pmatrix} 1 & \frac{1}{2} \\ 1 & \frac{1}{2} \\ 1 & -\frac{1}{2} \end{pmatrix} \Delta\vec{c} \\ &= \mathbf{H}\Delta\vec{c} = \mathbf{HT}\vec{s}, \end{aligned} \tag{12}$$

where $\mathbf{H}$ denotes our sampling operator, which reflects our capability to observe the state of the model. This yields $\Delta c_B = \Delta c_M = -4.6$ ppmv and $\Delta c_S = -0.1$ ppmv.

Our aggregated case consists of modeling only the global sources, then sampling them unevenly with our three stations. hence s_- represents the unresolved small-scale structure. This case is analogous to the situation depicted in Figure 1. In the following, we will frequently use a decomposition of the Jacobian matrix $\mathbf{J} = \mathbf{HT}$ defined by (12) into a column $\mathbf{J}_+$ multiplying the resolved s_+ component and one column $\mathbf{J}_-$ multiplying the unresolved s_- component. Using the definitions (11) and (12), we obtain their explicit form

$$\begin{aligned}\mathbf{J}\vec{s} &= \mathbf{J}_+ s_+ + \mathbf{J}_- s_- \\ &= \frac{\Delta t}{M}\begin{pmatrix}1\\1\\1\end{pmatrix} s_+ \\ &\quad + \frac{1}{2\kappa M}(1 - e^{-2\kappa\Delta t})\begin{pmatrix}1\\1\\-1\end{pmatrix} s_- \ . \qquad (13)\end{aligned}$$

4.3. Inversions

In the following, we will use the simulated concentration values of section 4.2 as pseudo-observations and try to recover from them the proper mean source. We therefore apply the inversion formula (4), and assume uncorrelated observational uncertainties with a standard deviation of $\sigma(d_0) = 1$ ppmv.

4.3.1. Demonstration of the effect. Aggregating the sources in this two-box model in the simplest possible way is by directly summing sources. This form of aggregation assumes a uniform source distribution, like the **U** cases in section 3. The unknown is the global source magnitude s_+, and the low-resolution Jacobian is $\mathbf{J}_+$. Using the pseudo-data, (4) yields an estimate for the global source s_+ of

$$\begin{aligned}\hat{s}_+ &= [(\mathbf{J}_+)^T(\mathbf{J}_+)]^{-1}(\mathbf{J}_+)^T \Delta\vec{c}_{\text{mod}} \\ &= \frac{M}{3\Delta t}\begin{pmatrix}1 & 1 & 1\end{pmatrix}\Delta\vec{c}_{\text{mod}} \ . \qquad (14)\end{aligned}$$

This yields an estimate of $\hat{s}_+ = -6.6$ Gt C, which is larger than the true sink of 5 Gt C by 1.6 Gt C or 32%, i.e., the aggregation error $\hat{s}_+ - s_+ = 1.6$ Gt C.

Note that the estimated source is too negative, reflecting the sampling bias toward the large sink in the Northern Hemisphere in this season. This demonstrates the combined roles of non-uniform sources and inhomogeneous sampling.

To demonstrate further the importance of inhomogeneous sampling, we repeat the inversion with one of the northern stations removed. In this case, reusing for convenience the symbols $\mathbf{J}_+$ and $\mathbf{J}_-$ for the resolved and unresolved components of this two-row Jacobian:

$$\begin{aligned}\hat{s}_+ &= [(\mathbf{J}_+)^T(\mathbf{J}_+)]^{-1}(\mathbf{J}_+)^T\begin{pmatrix}\Delta c_M\\ \Delta c_S\end{pmatrix} \\ &= \frac{M}{2\Delta t}\begin{pmatrix}1 & 1\end{pmatrix}\begin{pmatrix}\Delta c_M\\ \Delta c_S\end{pmatrix} \ , \qquad (15)\end{aligned}$$

which yields the true global source of 5 Gt C. Unlike the previous inversion, here the inversion formula performs proper averaging of the concentrations in both hemispheres before transforming this average to a source estimate. "Proper" averaging here means that there is no sampling bias.

A more formal way of achieving the same effect would be to use the average Northern Hemisphere concentration (with the same weight as the single Southern Hemisphere observation) to estimate the global source. This would be formalized by assigning perfectly correlated uncertainties to both Northern Hemisphere observations. $\mathbf{C}(d_0)$ is singular in this case, with the average Northern Hemisphere concentration contributing information but not the two stations individually.

There are two things to note about the above solutions to the aggregation error. First, in both cases, we are using knowledge of atmospheric transport to solve the problem. We choose weights for the data, which reflect our knowledge of rapid intrahemispheric mixing. In a more realistic case this knowledge is embodied in a transport model. These weights for data also do not reflect only the observational uncertainty $\mathbf{C}(d_{0,\mathrm{obs}})$ in (6). We will see later that they rather reflect the uncertainty arising from uncertainty in unresolved source components, which is to be treated as a model error $\mathbf{C}(d_{0,\mathrm{mod}})$.

The above shows that removing the inhomogeneity of the network removes the aggregation error. On the other hand, doing some simple but cumbersome matrix algebra, one can verify that the inversion with an inhomogeneous network, but the full Jacobian yields the proper global source (as well as the proper source difference). Again this shows that it is only the combination of inhomogeneous sampling and unresolved sources that creates an aggregation error.

4.3.2. Recipe to reduce aggregation error. The ad hoc solutions that we applied to our two-box model point the way to a more general algorithm. We have seen that the aggregation error arises from biased (or inhomogeneous) sampling of the small-scale, unresolved source structure. We stress again that we generally will not know this small-scale source structure perfectly and we are trying to avoid the impact of errors in this structure. Put roughly, the algorithm consists of de-weighting those observations that may bias the estimate. *Trampert and Snieder* [1996] suggest an algorithm to adjust the weights of the respective data items to achieve this. In our context, the idea is as follows.

We can assign uncertainty to the small-scale or unresolved components of the source field. Since the prescribed source shape can be considered a part of the model, errors in this shape can be considered a model error. The extra uncertainty arising from the unknown size of this error enters the inversion procedure on the data side, as explained in (6). It is derived by propagating the uncertainty in the small-scale shape, i.e., the s_- direction via the Jacobian to $\mathbf{C}(d_{0,\mathrm{mod}})$ on the data side. In the case of a transport model this propagation will, for example, assign large errors to observations taken near highly uncertain sources and hence de-weight them. Similarly, the propagation will add a strong correlation between uncertainties in two observations that sample the same small-scale structure. Usually, such observations will be from closely spaced stations. The procedure will reduce the combined impact of the two observations, thus reducing potential bias.

The uncertainty in the unresolved or small-scale components can be extracted from the a priori complete source covariance matrix $\mathbf{C}(\vec{s}_0)$ by means of a projection operator. In (7) we defined a mapping from the high-resolution source space (in that case the resolution of the transport model) to a subspace spanned by the patterns we are using. The projection onto the unresolved or small-scale patterns is the compliment of the operator defined in (7). In our two-box example it is defined as

$$\mathbf{P}_- = \begin{pmatrix} 0 \\ 1 \end{pmatrix} \begin{pmatrix} 0 & 1 \end{pmatrix} = \begin{pmatrix} 0 & 0 \\ 0 & 1 \end{pmatrix} . \qquad (16)$$

The extra uncertainty is then

$$\begin{aligned} \mathbf{C}(d_{0,\mathrm{mod}}) &= \mathbf{J}\mathbf{P}_-\mathbf{C}(\vec{s}_0)(\mathbf{J}\mathbf{P}_-)^T = \mathbf{J}_-\sigma(s_-)^2\mathbf{J}_-{}^T \\ &= [\frac{1}{2M\kappa}(1-e^{-2\kappa\Delta t})\sigma(s_-)]^2 \\ & \quad \begin{pmatrix} 1 \\ 1 \\ -1 \end{pmatrix} \begin{pmatrix} 1 & 1 & -1 \end{pmatrix} . \qquad (17) \end{aligned}$$

Note that $\mathbf{C}(d_{0,\mathrm{mod}})$ contributes to the uncertainty in the direction of c_- but also to that of c_+. This demonstrates the so-called leakage discussed by *Trampert and Snieder* [1996].

The structure of $\mathbf{C}(d_{0,\mathrm{mod}})$ shows that the additional uncertainties among the northern observations are completely correlated (and the uncertainties of any northern observation to the southern observation is completely anti-correlated). This is consistent with the ad hoc algorithm sketched above, with the advantage that it can be applied in more complex circumstances. $\mathbf{C}(d_{0,\mathrm{mod}})$ depends on the exchange rate and on the uncertainty in the source difference. If the exchange rate was large, $\mathbf{C}(d_{0,\mathrm{mod}})$ would be small and the observational uncertainty ($\mathbf{C}_{\mathrm{obs}}$) would dominate. This makes sense because a large exchange rate would reflect a well-mixed atmosphere and more equal weights for all three observations are appropriate.

The magnitude of $\mathbf{C}(d_{0,\mathrm{mod}})$ depends on the uncertainty for s_-. Independent uncertainties of 100% for s_1 and s_2 would yield an uncertainty of $\sigma(s_-)^2 = 30.5$ Gt C^2. In this case, $\mathbf{C}(d_{0,\mathrm{mod}})$ has the form of (17), with entries of the absolute value of 4.3 ppmv^2. This is the only uncertainty due to model error we consider. According to (6) we calculate the data uncertainty for (4) by adding $\mathbf{C}(d_{0,\mathrm{mod}})$ to $\mathbf{C}(d_{0,\mathrm{obs}})$, which we had assumed diagonal with entries of 1 ppmv^2. Applying (2) then yields an estimate of $\hat{s}_+ = -5.2$ Gt C. That is, the aggregation error is reduced from 32% ∼4%. Assuming instead uncertainties of 5 Gt C for both the northern and the southern source translates to an uncertainty of $\sigma(s_-)^2 = 50$ Gt C^2. Applying (2) then yields an estimate of $\hat{s}_+ = -5.1$ Gt C. That is, the aggregation error is reduced to 2%. Note that the aggregation error is not entirely antiproportional to the uncertainty of s_-, since s_- determines only one summand in the sum in (6). In particular, for this reason, the aggregation error cannot become infinitely large if the extra uncertainty is assumed to be lower and lower. In our setup the maximal aggregation error is 32%, as shown in section 4.3.1.

5. Reducing the Aggregation Error

In this section we apply the algorithm demonstrated in section 4 to the global CO_2 problem described in section 3. First, we discuss the extra data uncertainty caused by unresolved small-scale source components. Second, we carry out a number of inversions in which this additional uncertainty is added to the usual data uncertainty.

Appendix A describes the technicalities of computing the extra data uncertainty from the a priori uncertainty of the fluxes. For our computation we take this a priori uncertainty from the study of *Kaminski et al.* [1999b]. They specify a separate and uncorrelated uncertainty for the flux into each grid cell at each time step. Their uncertainties have some minimum value except in deserts or over ice-covered regions. The variances on land are the sum of those of net primary productivity, respiration, and land use change. For these processes, given the flux values based on process models of the terrestrial biosphere and the ocean carbon cycle as well as land use change statistics, they assumed uncertainties of 50%, 50%, and 100%, respectively.

Figure 4.

For our standard case U18, Figure 4 shows this extra data uncertainty for a number of sites. Alert (ALT) and Point Barrow (BRW) in Alaska are close to strong but unresolved biospheric sources. These sources are maximal in summer, so the extra uncertainty reaches a maximum in this season. The extra uncertainty is ∼ 1.5 ppmv, but only 0.4 ppmv during winter. At Cape Meares in Oregon (CMO), which is farther south, the biospheric activity lasts longer, and hence the period of high extra uncertainty is extended compared to Alaska. In contrast, places that are remote from the large surface sources, like the stations on Mauna Loa (MLO) on Hawaii, on Niwot Ridge (NWR) in the Rocky Mountains, or at the south pole (SPO), have a lower extra uncertainty of order 0.2 to 0.4 ppmv. The effect of remoteness from the sources is well illustrated by comparing MLO to the station at Cape Kumukahi (KUM), which is also on Hawaii but at sea level: at KUM the extra uncertainty is $\sim$ 2-3 times larger than at MLO.

Table 2.

To summarize the information at each station, Table 2 lists the annual mean of the additional weights and a mean value over all stations. We have added the numbers for cases with shaped patterns and 54 regions. As for the aggregation error described in section 3, we obtain the largest extra uncertainties for our standard case U18. The extra uncertainty is slightly reduced (by $\sim$ 10%) when using shaped patterns and reduced by $\sim$ 25% when using 54 regions. Using shaped patterns and 54 regions is not as efficient as using 54 uniform patterns but better than using 18 shaped patterns. As with the aggregation errors in section 3, the difference in moving from uniform to shaped patterns between the two resolutions is interesting. Several factors interact to make the interpretation difficult. First, the similarity between the structure of the uncertainty at full-resolution and the shape of the chosen basis functions determines how large the unresolved (small-scale) component of the uncertainty will be. This can be illustrated by a simple example. Imagine a small-scale structure with a large and a small a priori source component, and individual uncertainties proportional to the source strengths. The covariance of the source uncertainty would then have a large eigenvalue in the direction of the large source and a small one in the direction of the small source. In the uniform pattern case, both the resolved sum and the unresolved difference direction would have the same mean uncertainty. In the case with patterns shaped like the sources, most of the uncertainty would project on the resolved direction, and not much uncertainty would remain for the unresolved direction. Hence judging from this effect only, we would expect more extra data uncertainty in the uniform pattern case, provided the uncertainties are roughly proportional to fluxes. The transport of the unresolved source uncertainty is offsetting this advantage of shaped patterns. In the uniform pattern case the unresolved direction is a source difference, which is hardly seen, at least by remote stations. By contrast, with the shaped pattern case the unresolved direction has an average component. This component is observable at remote stations.

The mean of the residual standard deviations for these stations is also given in Table 2. It is taken from *Globalview–CO2* [1999]. The values are averaged over the period 1990–1995 where observations are available. These uncertainties are calculated as the standard deviation of the residuals of the flask measurements and the smooth curve used to interpolate them in time. They are hence a measure of temporal variability. Despite their quite different genesis, the two sets of uncertainties show similar structure, particularly in the Northern Hemisphere. A possible reason for this is that both sets are influenced by small-scale source structure. For the model-computed uncertainties this is clear from their construction (Appendix A). In contrast, the temporal variability in the observed CO_2 concentration could be due to temporal variations in transport acting on small-scale spatial variability in sources. We can think of the temporal variation in transport as allowing us to sample different parts of the small-scale source pattern. Exceptions to the agreement are the elevated site at Niwot Ridge, Colorado, (NWR) where the model shows little impact from local sources, and Ragged Point, Barbados (RPB), in which the model shows a substantial impact of local sources although the residual standard deviation is small. The NWR result is likely to be caused by difficulties in representing the sharp topography in a low-resolution model, meaning that the site is disconnected from the surface. Another reason for the disagreement is that in our model we do not mimic the data selection procedure, which is applied in order to reject air masses that are subject to strong local influence.

We have repeated our standard inversion U18 but added the extra uncertainty derived above to the 0.5 ppmv observational uncertainty. Since the covariance in the extra uncertainty of different observational items is small, for convenience we only included the diagonal terms. As networks become more dense, this simplification will become less acceptable. Figure 5 shows the annual mean of the aggregation error for this inversion, which is reduced compared to the the inversion without the extra uncertainty (see Figure 3).

Figure 5.

Table 3.

We also applied the same algorithm to the other cases in Table 1. Table 3 lists the same diagnostics that we had previously computed for the case without extra uncertainty. Comparing Tables 2 and 3 shows that in all cases all diagnostics have improved (except for the minimum difference in P18W, which got slightly worse). We focus in the discussion on the maximum absolute difference and the area-weighted rms difference. In the standard case and its counterpart with shaped patterns (U18 and P18), inclusion of the extra uncertainty reduced both diagnostics by more than half. In the cases with modified observational uncertainty, (the “W” cases) the initial aggregation error was much smaller. Including the extra uncertainty only reduced it by about a third for the uniform pattern case (U18W) and a quarter for the shaped pattern case (P18W). The most likely reason is the similarity in the data uncertainty from unresolved sources and that from neglecting interannual variability. This is similar to the case of the uncertainties from *Globalview–CO2* [1999].

In the 54-region inversions the initial aggregation error was much smaller than in the respective 18-region cases. Nevertheless, the inclusion of extra uncertainty succeeded in reducing the aggregation error by about one third.

6. Summary and Conclusion

We have carried out a set of atmospheric transport inversions for CO_2, which use the Jacobian matrix of a three-dimensional transport model to solve for the unknown magnitudes of 18 or 54 prescribed surface flux patterns, aggregating the fluxes over large regions. By comparing the fluxes to the ones inferred by an inversion on the grid of the underlying transport model, we were able to quantify errors due to such aggregation. Unfortunately, in many cases these errors are of the same order of magnitude as the fluxes themselves. For computational reasons, however, for many potential inversion studies aggregation will be unavoidable.

Reducing the degree of aggregation by moving from 18 to 54 regions about halves the error, which suggests using a resolution as high as computationally feasible. On the other hand, the maximum resolution needed is that which still leaves the Jacobian among neighboring flux components non-uniform. In this context it is important to note that in our model we did not mimic the observational data selection procedure, which would have made the Jacobian more uniform because it would have reduced the impact of local fluxes.

Since the focus of our study was not to infer the partition of land and ocean uptake, or land uptake of different continents, it was not necessary to choose basis functions that separate land and sea or among continents as is typical in inversion studies [*Bousquet et al.*, 1999; *Rayner et al.*, 1999]. Examining instead the aggregation for a set of non-uniformly shaped basis functions, which within our regular aggregation domains have a more realistic shape as suggested by process models, however, was an important test. Not only do these shapes take land-sea differences into account but also huge intracontinental variations in the fluxes, e.g., between forests and deserts. Switching to these shaped basis functions does not show a unique effect on the error. While for the 18-region case the aggregation error was halved, it increased by $\sim$ 50% in the 54-region case.

Determining a set of patterns that, for a given network, reduces the aggregation error is a task for further investigation. An even greater challenge will be to decide both the network and the patterns that for a specified region (or a number of regions simultaneously) yield the most accurate flux estimate. We introduced a simple two-box model to demonstrate how viewing errors in unresolved flux components as model errors can help to reduce the aggregation error. The transport model's full-resolution Jacobian matrix maps the uncertainty in the unresolved flux components to an extra uncertainty, i.e., a covariance matrix, on the data side that accounts for this model error. For the three-dimensional model this extra uncertainty is as large as 3.5 ppmv, which, however, depends on the assumptions for the uncertainty in the unresolved fluxes and needs further quantification. Even a recipe as crude as adding only the extra variances (i.e., only the diagonal elements) to the observational ones considerably reduces the aggregation error. Hence for any low-resolution inversion we recommend adding this additional uncertainty. The high-resolution Jacobian needed to compute the extra uncertainty and the low-resolution one used for the inversion need not be computed with the same transport model. Adding the extra uncertainty on the data side yields an increased uncertainty in the inferred flux fields but the alternative is a serious risk of large biases.

Appendix A: Detailed Algorithm Description

In this appendix we give a detailed description for the generation of the extra data uncertainty due to unresolved source components for use in an atmospheric tracer inversion. The aim is that other workers can apply the algorithm without dealing with the full background provided in the text. In order to compute $\mathbf{C}(d_{0,\mathrm{mod}})$ from (6) we require three inputs: (1) a set of patterns for whose magnitudes we wish to solve, (2) a high-resolution description of the prior uncertainty, and (3) a Jacobian matrix mapping the fluxes on the high-resolution grid to the chosen observational network.

The algorithm is in two steps. First, we must calculate the prior flux uncertainty, which is not resolved by our chosen patterns; second, we must project this uncertainty into an uncertainty on the data side, $\mathbf{C}(d_{0,\mathrm{mod}})$.

The patterns can be expressed as a series of vectors $\mathbf{p_i}$, where each component quantifies the flux in a particular cell of the transport model grid (for any of the disjoint patterns used in section 3, most of the components are 0). For convenience, we rescale and rotate the patterns to have unit length, i.e., $\mathbf{p_i}^T\mathbf{p_i} = 1$, and be orthogonal, i.e., $\mathbf{p_i}^T\mathbf{p_j} = 0$ for $i \neq j$ (the patterns in section 3 are orthogonal, because the regions are disjoint).

It is easy to show that the matrix defined by

$$\mathbf{P}_+ = \sum \mathbf{p_i}\mathbf{p_i}^T \tag{A1}$$

is a projection operator, which, although acting in the space of the high-resolution fluxes, extracts only components in the directions resolved by the patterns. The projector on the remaining (unresolved) directions $\mathbf{P}_-$ is defined by

$$\mathbf{P}_- = \mathbf{I} - \mathbf{P}_+ \quad . \tag{A2}$$

We can now calculate $\mathbf{C}(d_{0,\mathrm{mod}})$ by the usual rules for propagating covariances:

$$\mathbf{C}(d_{0,\mathrm{mod}}) = \mathbf{J}\mathbf{P}_-\mathbf{C}(\mathbf{s_0})\mathbf{P}_-^T\mathbf{J}^T \tag{A3}$$

We are now left with a computational issue. For the dimensions of our problem, $\mathbf{P}_-$ is approximately a 10,000 × 10,000 matrix, which we do not want to precompute and store. Further, the symmetry in (A3) is obvious and, owing to the diagonal structure of $\mathbf{C}(\mathbf{s_0})$, easy to exploit by

$$\mathbf{C}(d_{0,\mathrm{mod}}) \quad = \quad \mathbf{W}\mathbf{W}^T, \qquad \text{(A4)}$$

where $\mathbf{W}$ is defined by

$$\mathbf{W} \quad = \quad \mathbf{J}\mathbf{P}_-[\mathbf{C}(\mathbf{s_0})]^{1/2}. \qquad \text{(A5)}$$

Using the definition of P_- we obtain

$$\mathbf{W} \quad = \quad \mathbf{J}[\mathbf{C}(\mathbf{s_0})]^{1/2} - \sum \mathbf{J}\mathbf{p_i}\mathbf{p_i}^T[\mathbf{C}(\mathbf{s_0})]^{1/2}. \qquad \text{(A6)}$$

This means the propagation of the uncertainty from each pattern can be considered separately, and the whole matrix $\mathbf{P}_-$ need never be calculated.

Acknowledgments. The authors wish to thank Michael Voßbeck for producing the GrADS plots and Rachel Law for helpful comments on the manuscript. This study was carried out with the support of the Bundesministerium für Bildung und Forschung (BMBF) contract 01LA9898/9 as well as the support of the Australian government through its Cooperative Research Centres Programme.

References

Bousquet, P., P. Ciais, P. Peylin, M. Ramonet, and P. Monfrey, Inverse modeling of annual atmospheric CO_2 sources and sinks, 1, Method and control inversion, *J. Geophys. Res.*, *104*, 26,161–26,178, 1999.

Brown, M., Deduction of emissions of source gases using an objective inversion algorithm and a chemical tranport model, *J. Geophys. Res.*, *98*, 12,639–12,660, 1993.

Denning, A. S., et al., Three-dimensional transport and concentration of SF_6: A model intercomparison study (TransCom 2), *Tellus*, *51B*, 266–297, 1999.

Enting, I. G., T. M. L. Wigley, and M. Heimann, Future emissions and concentrations of carbon dioxide: Key ocean/atmosphere/land analyses, *Tech. Pap. 31*, CSIRO Div. of Atmos. Res., Aspendale, Victoria, Australia, 1994.

Enting, I. G., C. M. Trudinger, and R. J. Francey, A synthesis inversion of the concentration and δ^{13}C of atmospheric CO_2, *Tellus, Ser. B*, *47*, 35–52, 1995.

Fan, S., M. Gloor, J. Mahlman, S. Pacala, J. Sarmiento, T. Takahashi, and P. Tans, A large terrestrial carbon sink in north america implied by atmospheric and oceanic carbon dioxide data and models, *Science*, *282*, 442–446, 1998.

Fung, I., J. John, J. Lerner, E. Matthews, M. Prather, L. P. Steele, and P. J. Fraser, Three-dimensional model synthesis of the global methane cycle, *J. Geophys. Res.*, *96*, 13,033–13,065, 1991.

Globalview–CO2, *Cooperative Atmospheric Data Integration Project - Carbon Dioxide* [CD-ROM], NOAA/CMDL, Boulder, Colo., 1996.

Globalview–CO2, *Cooperative Atmospheric Data Integration Project - Carbon Dioxide* [CD-ROM], NOAA/CMDL, Boulder, Colo., 1999.

Heimann, M., The global atmospheric tracer model TM2, *Tech. Rep. 10,* Max-Planck-Inst. für Meteorol., Hamburg, Germany, 1995.

Hein, R., P. J. Crutzen, and M. Heimann, An inverse modeling approach to investigate the global atmospheric methane cycle, *Global Biogeochem. Cycles*, *11*, 43–76, 1997.

Houweling, S., T. Kaminski, F. Dentener, J. Lelieveld, and M. Heimann, Inverse modelling of methane sources and sinks using the adjoint of a global transport model, *J. Geophys. Res.*, *104*, 26,137–26,160, 1999.

Kaminski, T., M. Heimann, and R. Giering, A coarse grid three-dimensional global inverse model of the atmospheric transport, 1, Adjoint model and Jacobian matrix, *J. Geophys. Res.*, *104*, 18,535–18,553, 1999a.

Kaminski, T., M. Heimann, and R. Giering, A coarse grid three-dimensional global inverse model of the atmospheric transport, 2, Inversion of the transport of CO_2 in the 1980s, *J. Geophys. Res.*, *104*, 18,555–18,581, 1999b.

Keeling, C. D., S. C. Piper, and M. Heimann, A three-dimensional model of atmospheric CO_2 transport based on observed winds, 4, Mean annual gradients and interannual variations, in *Aspects of Climate Variability in the Pacific and the Western Americas*, *Geophys. Monogr. Ser.*, vol. 55, edited by D. H. Peterson, pp. 305–363, AGU, Washington, D. C., 1989.

Law, R. M., et al., Variations in modelled atmospheric transport of carbon dioxide and the consequences for CO_2 inversions, *Global Biogeochem. Cycles*, *10*, 783–796, 1996.

Peylin, P., P. Bousquet, P. Ciais, and P. Monfray, Differences of flux estimates based on a time-independent versus a time dependent inversion method, in *Inverse Methods in Global Biogeochemical Cycles, Geophys. Monogr. Ser.*, vol. 114, edited by P. Kasibhatla et al., pp. 295–309, AGU, Washington, D. C., 2000.

Rayner, P. J., I. G. Enting, R. J. Francey, and R. L. Langenfelds, Reconstructing the recent carbon cycle from atmospheric CO_2, $\delta^{13}C$ and O_2/N_2 observations, *Tellus, Ser. B, 51*, 213–232, 1999.

Rayner, P., R. Giering, T. Kaminski, R. Ménard, R. Todling, and C. Trudinger, Exercises, in *Inverse Methods in Global Biogeochemical Cycles*, *Geophys. Monogr. Ser.*, vol. 114, edited by P. Kasibhatla et al., pp. 81–105, AGU, Washington, D. C., 2000.

Tans, P. P., A note on isotopic ratios and the global atmospheric methane budget, *Global Biogeochem. Cycles*, *11*, 77–81, 1997.

Tans, P. P., I. Y. Fung, and T. Takahashi, Observational constraints on the global atmospheric CO_2 budged, *Science*, *247*, 1431–1438, 1990.

Tarantola, A., *Inverse Problem Theory - Methods for Data Fitting and Model Parameter Estimation*, Elsevier Sci., New York, 1987.

Trampert, J., and R. Snieder, Model estimations biased by truncated expansions: Possible artifacts in seismic tomography, *Science*, *271*, 1257–1260, 1996.

I. G. Enting and P. J. Rayner CSIRO Atmospheric Research, PMB 1, Aspendale, Victoria 3195, Australia. (peter.rayner@dar.csiro.au; ian.enting@dar.csiro.au)

M. Heimann, Max-Planck-Institut für Biogeochemie, Postfach 100164, D-07701 Jena, Germany. (mheimann@bgc-jena.mpg.de)

T. Kaminski, FastOpt, Martinistr. 21, D-20251 Hamburg, Germany. (thomas@fastopt.de)

(Received May 26, 2000; revised September 6, 2000;
accepted September, 15, 2000.)

Paper number 2000JD900581.
0148-0227/01/2000JD900581$09.00

Figure Captions

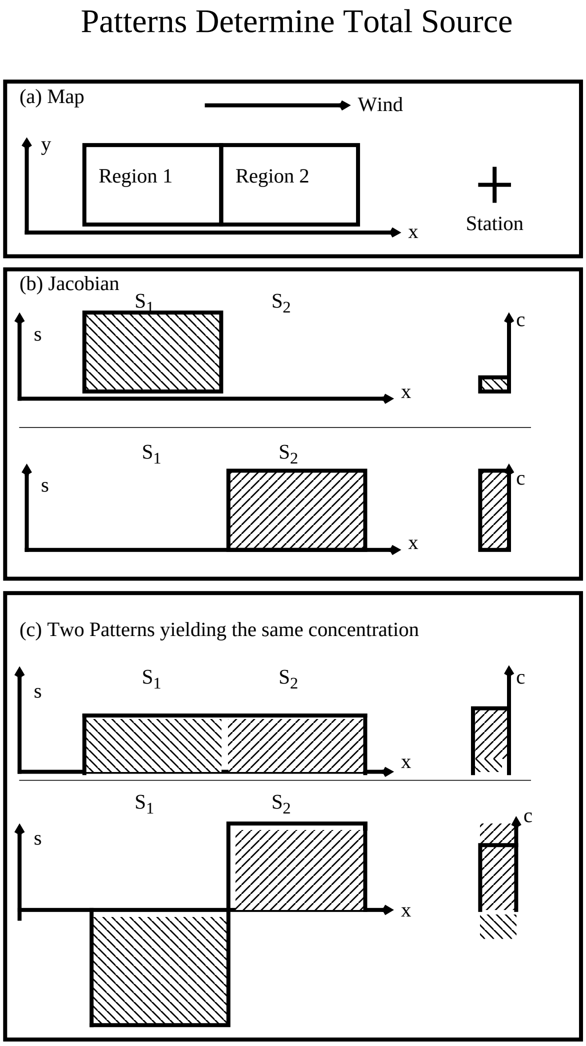

Figure 1. (a) An idealized situation of two regions upwind of an observational site. Since region 1 is farther upwind than region 2, for equal emissions S_1 and S_2, the source S_2 in region 2 has a higher impact on the concentration at the station. (b) Jacobian that quantifies this impact. (c) Two choices of emission patterns that yield the same concentration at the station. While for the first pattern the aggregation over both regions is a net source, for the second pattern is a net sink. Hence from the atmospheric information alone it is not possible to distinguish a net source from a net sink. This is determined by the additional information provided through choosing a pattern.

Figure 1. (a) An idealized situation of two regions upwind of an observational site. Since region 1 is farther upwind than region 2, for equal emissions S_1 and S_2, the source S_2 in region 2 has a higher impact on the concentration at the station. (b) Jacobian that quantifies this impact. (c) Two choices of emission patterns that yield the same concentration at the station. While for the first pattern the aggregation over both regions is a net source, for the second pattern is a net sink. Hence from the atmospheric information alone it is not possible to distinguish a net source from a net sink. This is determined by the additional information provided through choosing a pattern.

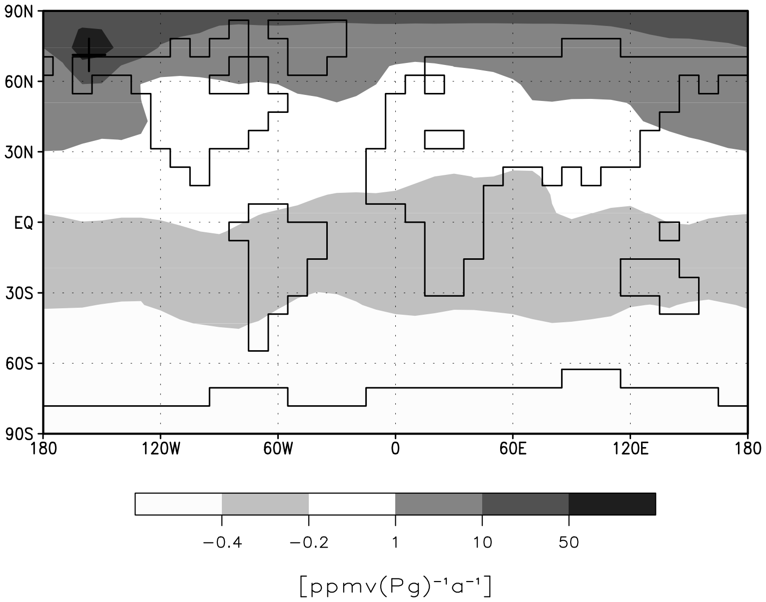

Figure 2. Influence map on TM2 grid for the January mean concentration at station BRW. Sensitivity of the simulated concentration with respect to potential fluxes within the same month as simulated by TM2 (see *Kaminski et al.* [1999a] for more details).

Figure 2. Influence map on TM2 grid for the January mean concentration at station BRW. Sensitivity of the simulated concentration with respect to potential fluxes within the same month as simulated by TM2 (see *Kaminski et al.* [1999a] for more details).

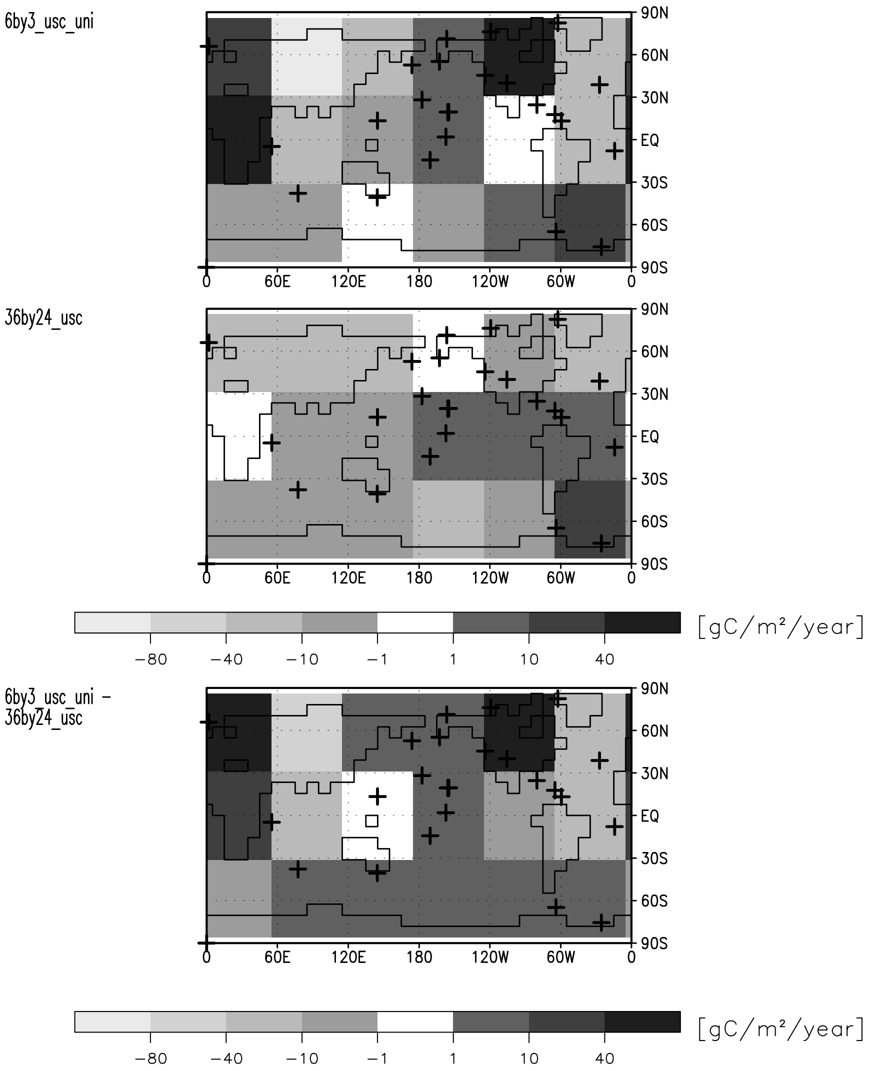

Figure 3. Annual mean of a posteriori values averaged over groups of 9 (zonally) × 6 (meridionally) TM2 grid squares (top) from an inversion on the aggregated grid (case 18), (middle) averaged after inversion of the TM2 grid (case R), and (bottom) their difference; in the difference plot, positive values quantify an enhanced source or a reduced sink in the aggregated inversion.

Figure 3. Annual mean of a posteriori values averaged over groups of 9 (zonally) × 6 (meridionally) TM2 grid squares (top) from an inversion on the aggregated grid (case 18), (middle) averaged after inversion of the TM2 grid (case R), and (bottom) their difference; in the difference plot, positive values quantify an enhanced source or a reduced sink in the aggregated inversion.

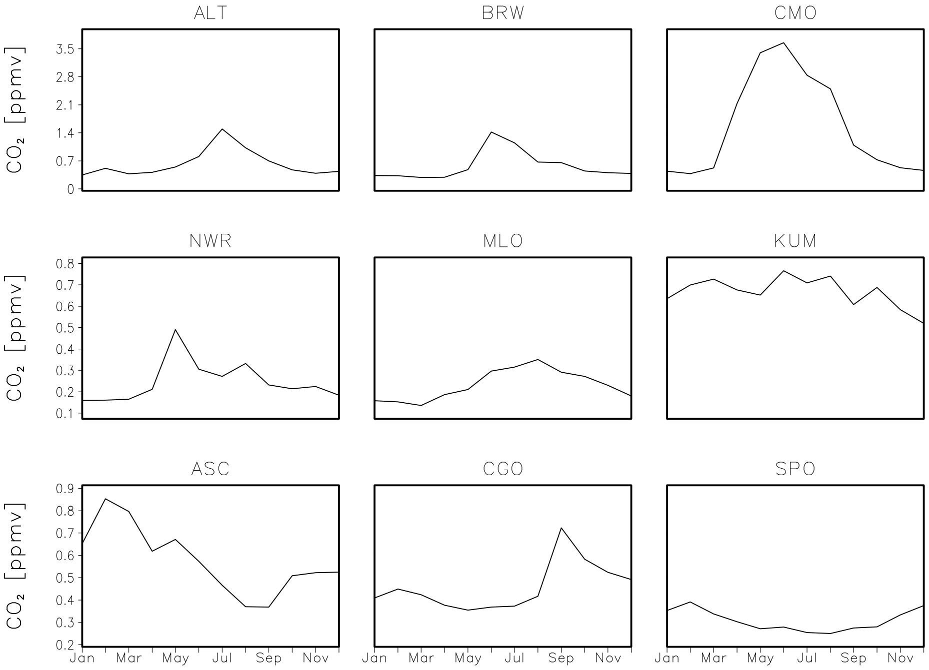

Figure 4. Extra data uncertainty (as standard deviation in ppmv) computed from uncertainty in the unresolved source components for the U18 case for Alert (ALT) and Point Barrow (BRW), Alaska; Cape Meares, Oregon (CMO); Niwot Ridge, Colorado, (NWR); Mauna Loa (MLO) and Cape Kumukahi (KUM), Hawaii; Ascension Island (ASC); Cape Grim, Tasmania (CGO); and South Pole (SPO).

Figure 4. Extra data uncertainty (as standard deviation in ppmv) computed from uncertainty in the unresolved source components for the U18 case for Alert (ALT) and Point Barrow (BRW), Alaska; Cape Meares, Oregon (CMO); Niwot Ridge, Colorado, (NWR); Mauna Loa (MLO) and Cape Kumukahi (KUM), Hawaii; Ascension Island (ASC); Cape Grim, Tasmania (CGO); and South Pole (SPO).

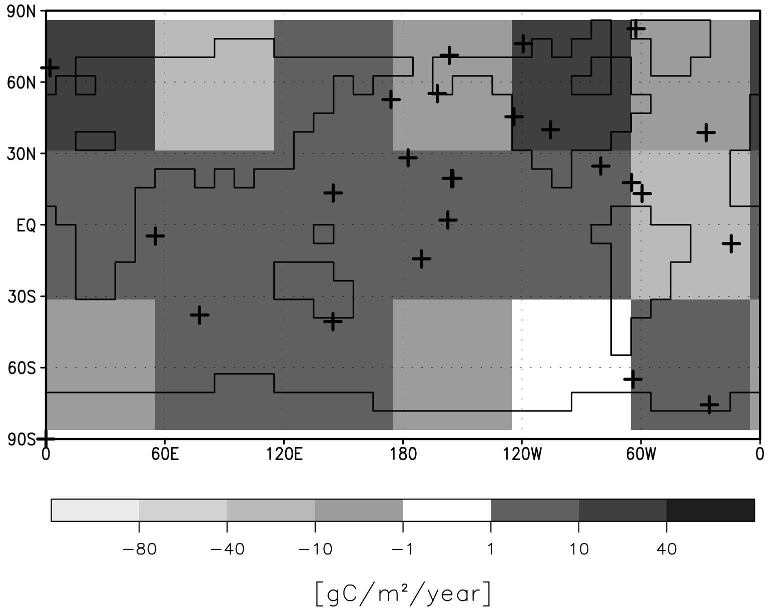

Figure 5. Annual mean of aggregation error for the U18 case. As in Figure 3 (bottom), but here the low-resolution inversion was carried out with extra uncertainty accounting for uncertainty in unresolved sources. Positive values imply a positive aggregation error.

Figure 5. Annual mean of aggregation error for the U18 case. As in Figure 3 (bottom), but here the low-resolution inversion was carried out with extra uncertainty accounting for uncertainty in unresolved sources. Positive values imply a positive aggregation error.

Tables

Table 1. Various Diagnostics of Aggregation Error for Six Different Setups of the Low-Resolution Inversion [a]

Identifier	Maximum Difference	Minimum Difference	Maximum Absolute	rms	rms Area-Weighted
U18	677.68	-931.24	931.24	66.94	90.39
P18	262.70	-536.49	536.49	35.99	47.42
U18W	619.10	-277.91	619.10	42.94	58.15
P18W	106.19	-176.93	176.93	15.65	22.03
U56	166.54	-256.66	256.66	52.51	26.78
P56	313.44	-342.23	342.23	72.84	36.70

[a] Identifiers are shown for low-resolution inversion, maximum positive error over all months and aggregation regions, minimum negative error, maximum absolute error, root mean squared (rms) error and, area-weighted rms error. All values are in g C $m^{-2}yr^{-1}$: positive values quantify an enhanced source or a reduced sink in the aggregated inversion. The maximum and minumum fluxes for the full-resolution inversion are –463 g C $m^{-2}yr^{-1}$ and +190 g C $m^{-2}yr^{-1}$. For the U18 case, the annual mean of the aggregation error is depicted in Figure 3.

Table 2. Annual Mean of Extra Data Uncertainty Due to Unresolved Sources at the Observational Sites [a]

Station	**U**18	**P**18	**U**54	**P**54	Globalview RSD
ALT	1.7481	0.7058	0.6282	0.5778	0.68
MBC	1.8424	0.7642	0.7860	0.6048	0.80
BRW	1.0819	0.9490	0.5721	0.6601	0.92
STM	1.0179	0.8681	0.5038	0.6920	0.95
CBA	0.6398	0.8574	0.5030	0.6668	1.10
SHM	0.6605	0.8409	0.5134	0.7178	0.81
CMO	1.9188	2.0691	1.5572	1.5309	1.81
AZR	0.5054	0.6601	0.4511	0.6261	1.31
NWR	0.3434	0.4862	0.2461	0.4228	1.14
MID	0.6209	0.7120	0.5471	0.6734	0.75
KEY	1.0855	1.0150	1.1291	0.9911	0.73
MLO	0.3231	0.4363	0.2318	0.4030	0.54
KUM	0.7234	0.8007	0.6673	0.7684	0.73
GMI	0.6052	0.7118	0.4546	0.6100	0.68
AVI	0.9870	0.7748	0.8500	0.8119	
RPB	1.3047	0.9682	1.0520	0.9738	0.44
CHR	0.5956	0.7015	0.5683	0.6450	0.23
SEY	0.9305	0.9293	0.9177	0.8609	0.82
ASC	0.9762	1.0188	0.5771	0.9432	0.58
SMO	0.5594	0.6804	0.4444	0.6485	0.41
AMS	0.5614	0.7220	0.4626	0.6829	
CGO	0.5386	0.6293	0.4578	0.5874	0.23
PSA	0.4945	0.6848	0.3509	0.5629	0.16
HBA	0.9519	0.5608	0.3261	0.4797	0.18
SPO	0.6828	0.5192	0.3085	0.4520	0.41
average	0.867956	0.802628	0.604248	0.703728	

[a] As standard deviation in ppmv. Identifier for the station location is given. Extra uncertainties for four setups are given and contrasted to residual standard deviations (RSD) from *Globalview–CO2* [1999].

Table 3. Various Diagnostics of Aggregation Error for Six Different Setups of the Low-Resolution Inversion but With Extra Data Uncertainty Taken Into Account [a]

Identifier	Maximum Difference	Minimum Difference	Maximum Absolute	rms	rms Area-Weighted
U18	337.63	-187.01	337.63	26.50	36.59
P18	135.69	-83.11	135.69	13.83	19.81
U18W	370.98	-111.68	370.98	26.28	35.77
P18W	129.17	-62.42	129.17	12.28	18.30
U56	129.20	-136.73	136.73	32.24	17.19
P56	210.53	-189.32	210.53	46.45	27.34

[a] See Table 1 for more details. All values are in g C $m^{-2}yr^{-1}$.

Paper number 2000JD900581

This paper explores the consequences of resolution of surface fluxes on synthesis inversions of carbon dioxide. Synthesis inversion divides the Earth's surface into a set of regions and solves for the magnitudes of fluxes from these regions. The regions are generally quite large. By considering an inversion performed at the resolution of the underlying transport model we show that the aggregation to large regions can cause significant differences in the final results, with errors of the same order of magnitude as the fluxes themselves. Using a simple model, we derive an algorithm to reduce this error. This algorithm accounts for the extra data uncertainty that is caused by uncertainty in the small-scale flux components. In the spatial synthesis inversion this extra data uncertainty reaches a maximum value of 3.5 ppmv. Accounting for it can halve the aggregation error. We provide suggestions for dealing with this problem when high-resolution inversions are not feasible.